steel research international

www.steel-research.de

REVIEW

Review on Modeling and Simulation of Electroslag Remelting

Abdellah Kharicha,* Ebrahim Karimi-Sibaki, Menghuai Wu, Andreas Ludwig, and Jan Bohacek

The Electroslag Remelting (ESR) is an advanced technology for the production of high quality materials, for example, hot work tool steels or nickel base alloys. In the past years, several models are developed aiming to predict the way in which the operational parameters affect the structure and chemical composition of the final ESR ingot. Proper modeling of this process depends on the ability of the model to predict the Multiphysics resulting from the complex coupling between many physical phenomena. This review includes the main findings starting from the 1970's, with a special focus on the results obtained in the period of 1999–2017. The difficulties related to the poorly known physical properties of ESR slags are discussed. Then, the main achievements in the field of electromagnetism, fluid flow, heat transfer, and solidification are also summarized. The review finishes by presenting the special topics representing the actual scientific frontiers, such as the physics of mold current, the importance of multiphase phenomena, and the difficulties in predicting the electrode melting rate.

1. Introduction

Electroslag remelting (ESR) is a secondary metallurgical process aiming at further purification after completion of the primary extraction and refining operations. The process (**Figure 1**) is a method of refining a consumable metal electrode through a molten slag that is electrically heated. Thermal energy is supplied to the process through the Joule heating that results in remelting the primary electrode and formation of droplets. The droplets then pass through the slag and reach the liquid pool. The melt pool solidifies directionally and builds the high-grade ingot in a water-cooled mold.

It is not clear who invented the process although the earliest recorded reference to the principles of the process had been reported by Nickolai Slavyanov in 1892.[1,2] Armstrong[3] had conducted experiments on a small scale using a resistance heated slag to aid melting in 1928. Then, Hopkins[4,5] had melted a consumable electrode under a slag blanket in 1935. After World War II, Soviet scientists had developed electroslag welding process to improve metal quality and to mechanize the welding of vertical joints at the E. O. Paton Institute of Electric Welding in Kiev.[6] Furthermore, Soviet researchers published the first monographs on the topic of ESR in 1962, which were translated and published abroad.[7] Over past decades, the process has been developed to produce a variety of ferrous and non-ferrous alloys such as steel, nickel-based, and titanium-based super alloys. Diverse application areas exist for ESR products in tool steel, aircrafts, oil and chemical industries, thermal power station, nuclear power plant, and military technology. Nowadays, million tons of ESR ingots are produced in a wide range of sizes and weights in various countries such as Austria, Brazil, Canada, China, England, France, Germany, Hungary, Iran, Italy, Japan, Russia, Slovenia, South Korea, and USA.

Finely controlled solidification is a remarkable characteristic of the ESR process that leads to production of ingots with superior surface and internal quality. The expensive process of surface machining is not required for ESR ingots with smooth surfaces as they can be directly forged after completion of the ESR process.[8] The internal quality is highly dependent on the shape of melt pool, that is, the depth and thickness of mushy zone. The desired outcome of the ESR process is a shallow melt pool that promotes unidirectional (upwards) solidification of the ingot and subsequent formation of segregation minimalized alloys.[9,10] The degree of macrosegregation depends largely on the slope of the solidus/liquidus isotherms and solidification time, which is related to the mushy zone depth. In fact, long solidification time or deep mushy zone results in severe macrosegregation and subsequently inadequate mechanical properties, cleanliness, and

[*] Dr. A. Kharicha, Dr. E. Karimi-Sibaki, Prof. M. Wu
Christian Doppler Laboratory for Advanced Process Simulation of Solidification and Melting, Montanuniversitaet Leoben, Austria
Email: abdellah.kharicha@unileoben.ac.at
Dr. A. Kharicha, Prof. M. Wu, Prof. A. Ludwig, Dr. J. Bohacek
Chair of Simulation and Modeling of Metallurgical Processes, Montanuniversitaet Leoben, Austria

DOI: 10.1002/srin.201700100

Dr. Abdellah Kharicha has studied fundamental physics at Joseph Fourier University in Grenoble, France. He did his Master degree (in 1999) and his PhD (in 2004) at Institut National Polytechnique de Grenoble in France. Since 2008, Dr. A. Kharicha is a group leader at the Chair for "Simulation and Modelling of Metallurgical Processes" at Montauniversitaet Leoben in Austria. His main research interests are the modeling and simulation of phenomena related to engineering applications of magnetohydrodynamics and solidifcation.

Dr. Ebrahim Karimi Sibaki did his Master degree in 2011 at Chalmers University of Technology in Sweden, and PhD in 2016 at Montanuniversitaet Leoben in Austria. Currently, he is a member of Christian Doppler Laboratory for "Advanced Process Simulation of Solidification and Melting". His main research interests are the modeling and simulation of metallurgical processes involving magnetohydrodynamics and solidification.

Prof. Menghuai Wu did his Master degree in 1986 at Northwestern Polytechnical University in China, PhD degree in 2000 at the Foundry Institute, RWTH Aachen in Germany, and Habilitation (professorial cetificate) in 2008 at Montanuniversitaet Leoben in Austria, and became the head of Christian Doppler Laboratory for "Advanced Process Simulation of Solidification and Melting" in 2010. His main research interests are the modeling and simulation of solidification and related phenomena during different casting processes.

yield.[11–13] Therefore, the melt pool profile is often used as an indicator of the internal quality of the ingot. The liquid pool shape is governed by operating conditions such as electrical parameters, mold cooling system, slag/alloy properties, etc.

Hoyle[5] comprehensively described various aspects of the standard ESR process, such as required equipment, instrumentation, control, and operating practice. A schematic representation of the process including major components of electrode, slag, ingot and mold is illustrated in Figure 1. ESR molds, typically made of copper, are designed to contain the hot slag bath, to receive and

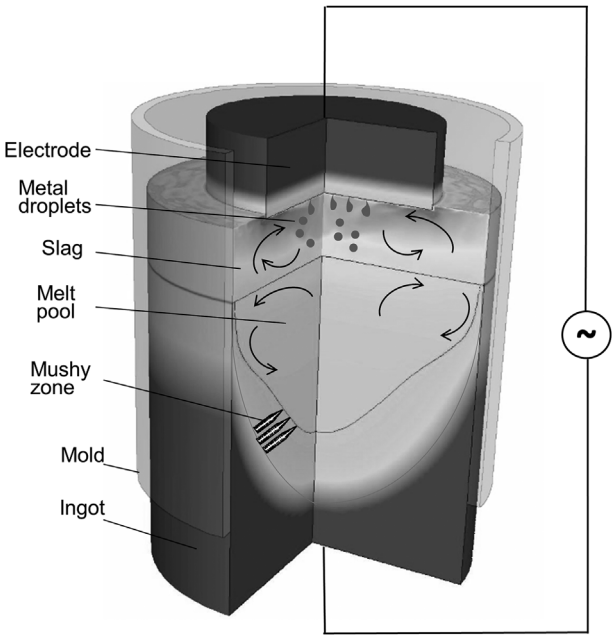

Figure 1. Schematic representation of the ESR process.

accumulate the molten metal, and to provide a suitably shaped vessel for the solidifying ingot. A substantial part of generated heat in the process is transferred through the mold wall to the cooling water. Furthermore, considerable amount of electric current flows through the mold. As such, special care must be taken to design an adequate mold which is capable of fulfilling all the tasks.[14,15] Principally, three different configuration of standard ESR plant exist: plant with retractable baseplate, static (live) mold, and short-collar/moveable (isolated) mold; each of them has particular fields of application.[16]

The complex ESR process involves a range of physical phenomena and their interactions: heat transfer with phase change taking place in melting of the electrode and solidification of the ingot, chemical and electrochemical reactions in the slag, and the interaction between the turbulent flow and electromagnetic field known as magnetohydrodynamics (MHD). Experimental analysis and measurements are quite difficult during the ESR process due to high degree of opacity of materials and involved high temperatures ($\approx$2000 K). One should consider that traditional trial and error approaches are prohibitively expensive especially for production of large ESR ingots. Therefore, it is necessary to develop mathematical models describing transport phenomena occurring in the whole process. Simulation tools can be effectively applied to get insight into the invisible phenomena. Computational fluid dynamics (CFD) is a very powerful technique that enables us to attain deeper knowledge of the ESR process. That is, of key importance for improving the technology, minimizing failure rate, and increasing productivity.

Unfortunately, it is impossible to describe all involving phenomena such as melting, solidification, magnetohydrodynamics (MHD), chemical, and electrochemical reactions in one single model. It is a major challenge to consider all physical phenomena, which occur at different length scales because of limitations in computational resources. The present paper starts by discussing the difficulties related to the poorly known physical properties of ESR slags. Then, a summary of the previously proposed numerical models are given. Due to its prime importance, the modeling of electromagnetic field is discussed in details. The main achievements in the field of fluid flow, heat transfer, and solidification are also summarized. The review finishes by presenting the special topics representing the actual scientific frontiers such as the physics of mold current, the importance of multiphase phenomena, chemistry, electrochemistry, and the difficulties in predicting the electrode melt rate.

2. Uncertainties on Physical Properties of ESR Slags

Properties of metallic alloys are relatively well-known compared to slags used in the ESR process. The slag is the core compound served to clean the metal by removing sulfur and non-metallic inclusions. Several chemical and electrochemical reactions take place in the slag aiming at further purification and refining of the metal.[17,18] The required heat is supplied into the process by passing electric current through the resistive slag layer (Joule heat). Furthermore, the slag protects the molten metal from direct contamination that might come from the surrounding atmosphere. A crust of solidified slag, called slag skin layer, forms a mold lining which separates molten slag and ingot from the mold.

For several decades, a large amount of research has been ongoing to explore the chemical mechanisms, which control the properties of ESR slags. It is beyond the scope of the current paper to address hundreds of books, monographs, and scientific papers which were reviewed elsewhere.[19,20] CaF_2-based slags are generally used since they have a high degree of chemical reactivity and low electrical conductivity. A conventional ESR slag is typically composed of a mixture of CaF_2 (30–70 wt%), Al_2O_3 (15–60 wt%), and CaO (15–60 wt%).[2] Most often, a small amount of SiO_2, TiO_2, and MgO are added to modify the reactivity of the slag that, in turn, influences the final compositions of Al, Ti, or Mg in the ingot.[21–24] Furthermore, the aforementioned oxides can change physical as well as physicochemical properties of the slag such as viscosity, density, etc.[19] For instance, a lubricative skin layer forms on the surface of a short collar (moveable) mold by addition of SiO_2 to the slag, that is, in favor of producing ingots with superior surface quality.[25] The physicochemical properties are dependent on both temperature and composition of the slag. Due to the difficulty of measurements at elevated temperature, a large uncertainty of the properties exists.[26] The following crucial slag properties are required for CFD modeling, which are extracted from literature: electric conductivity,[26–32] thermal conductivity,[27,33,34] viscosity,[19,26,27,35–37] density,[2,19,26,27,37–40] specific heat,[41] surface tension,[19,27,40,42] emissivity,[34,43] and liquidus/solidus temperature.[35,44] The physicochemical properties of the conventional slags can vary strongly as function of composition and temperature (**Table 1**). The properties of the solidified slag skin have rarely been investigated.[45] The thermal properties of solidified slag skin control the magnitude of heat loss from the liquid slag, as well as the level of thermal insulation between the ingot and the mold. Typical slag skin heat conductivity used in numerical models is $0.5\,W\,m^{-1}\,K^{-1}$. However recent measurements suggested that the actual value is in the range of $2–4\,W\,m^{-1}\,K^{-1}$.[45] Electrical conductivity of solid slags varies strongly with temperature, typically with an Arrhenius law. It can be assumed to be insulating at the room temperature, but not at elevated temperatures at which the thin slag skin is held during the process (≈800–1450 K). For a 50 Hz current and at a temperature of about 1000 K, private industrial measurements using impedance spectroscopy suggested conductivity in the range of $0.001–50\,\Omega^{-1}\,m^{-1}$. Considering the average value over its thickness, the electrical conductivity of slag skins should be in the range of $1–15\,\Omega^{-1}\,m^{-1}$. These suggestions should be taken with extreme care since the composition of the actual slag skin can differ strongly from that of the originally defined slag as a consequence of some segregation phenomena occurring inside the slag skin.

Electrical conductivity liquid ($\Omega^{-1}\,m^{-1}$)	50–300
Electrical conductivity solid ($\Omega^{-1}\,m^{-1}$)	10^{-3}–50
Thermal conductivity liquid ($W\,m^{-1}\,K^{-1}$)	4–50
Molecular thermal conductivity solid ($W\,m^{-1}\,K^{-1}$)	0.5–4
Viscosity (Pa s)	0.002–0.1
Density ($kg\,m^{-3}$)	2500–2900
Specific heat ($J\,kg^{-1}$)	900–1400
Surface tension ($N\,m^{-1}$)	0.1–1
Emissivity	0.8–0.9
Solidus temperature (K)	1300–1500
Liquidus temperature (K)	1600–1800

Table 1. Variation range of physicochemical properties of the conventional ESR slags.

3. Mathematical Modeling of Transport Phenomena

Over the past century, numerous mathematical models have been proposed to describe the fluid flow, heat transfer, and mass transfer in the ESR. First, models which can be found in literature are based on empirical data collected during operation. Willner et al.[46] had performed a multi-regression analysis of measurements to explore the relationship between electrode diameter, power input,

Involving physics	Calculation domains	Brief description of key model features	Ref.
Only thermal (solidification) field	Only ingot	Quasi steady state pool profile of the ingot and related solidification parameters such as depth of mushy zone, local solidification time (LST), and grain growth angle (GGA) were studied. Radial contraction and thermal stress on solidifying ingot were also studied.	[48,49,52,58,65,70,97,98]
	All possible regions	Pool profile of the ingot and related solidification parameters such as shrinkage of the ingot, secondary dendrite arm space (SDAS), LST, and GGA were studied. Temperature profile of the electrode, immersion depth and shape of electrode were investigated.	[50,51,54,55,60,61,95]
Only electromagnetic field	All possible regions	Effects of operational parameters of the process such as diameter of electrode or ingot, applied AC frequency, and slag resistance on distribution of electric current density and generated power were studied.	[62,69,72,85,90,92,107]
Coupled flow, electromagnetic fields	Slag and melt pool	Variations in distribution of electric current density influence the velocity field as well as the movement of slag-pool interface.	[53,66]
Coupled flow, thermal (solidification), electromagnetic fields	Only slag	The flow pattern is influenced by Lorentz and thermal buoyancy forces, size of droplets, thickness of the slag skin, melt rate of the electrode, and mold current.	[56,64,73,75,77,87,117]
	Slag and ingot	The flow in the slag and melt pool as well as pool profile of the ingot and related solidification parameters such as columnar to equiaxed transition (CET), LST, SDAS, and GGA are dependent on applied current, mode of current (AC or DC), generated power, fill ratio, size of droplets, skin thickness, and movement of slag-pool interface. Macrosegregation, probability of formation of freckles, and distribution of inclusions were addressed.	[57,63,67,68,71,74,76,78–83,88,89,93,94,96,99,101–105,110,111,113–114,108,109,116]
	All possible regions	The generated power, feeding velocity of the electrode, melt rate of the electrode, and the size of the system significantly influence thermal field in the electrode and slag.	[59,84,91,100,106,112,115]

Table 2. A summary of the mathematical models for fluid flow, heat transfer, electromagnetism, melting of the electrode, and solidification of the ingot in the ESR process.

feeding velocity, specific power, and pool depth in the ESR. An excellent review of the topic at the date of 1999 was previously given by Hernandez-Morales et al.[47] Here, the review focuses on the latest developments made in the period of 1989–2016.

Here, an extensive reviews of mathematical models of fluid flow, electromagnetism, heat transfer, and solidification in the ESR are given.[48–117] Because of their principle importance, only equations of the electromagnetic fields are discussed in details. A summary of models is listed in **Table 2** according to the investigated phenomena, as well as involved domain of modeling. Furthermore, key features of the model for each group of references are briefly described.

3.1. Electromagnetic Field

The thermic and the hydrodynamic of both slag and melt pool are strongly influenced by the electromagnetic field in the ESR process. As such, an accurate prediction of the electromagnetic field is the very first step in modeling of the process. After computing the electromagnetic field, distributions of Lorentz force and Joule heat can be obtained, which are source terms for momentum and energy equations, respectively.[105] The origin of the Lorentz force is the interaction between the electric current and the self-induced magnetic field in the system. Furthermore, the process by which the passage of an electric current through a conductor releases heat is known as Joule or resistive heating.

Dilawari et al.[53] have shown that the magnetic Reynolds number is sufficiently low to neglect the effect of flow convection on magnetic field distribution. However the flow can still act on the electromagnetic field through the advection of the liquid electric properties. For instance, the movement of slag-melt pool interface and dripping of droplets through the slag can dynamically modify electromagnetic field.[83] It is acceptable to assume that the magnetic field is dominantly in azimuthal direction. In many situations and for the sake of simplicity, we can ignore the effects of slag-pool interface movement and of the droplets on the global electromagnetic field. Thus, a 2D axisymmetric model was found enough to describe the average electric current distribution in the ESR.[79] In the literature, two different approaches were suggested to calculate the electromagnetic field: the most widely used is the one based on magnetic induction formulation,[88,105] and other is based on vector potential-scalar potential formulation.[100,106,118,119]

3.1.1. Method Based on the Magnetic Induction

The use of AC implies that magnetic and electric fields are coupled; hence, the phenomena are governed by the four Maxwell equations. Several assumption are usually made: (i) due to presence of high temperatures, magnetization is negligible, (ii) as already stated the magnetic Reynolds number is very small thus the flow does not transport the magnetic field, (iii) the current displacement is much weaker than the electric conduction. Considering an axisymmetric system and in the absence of an external field, the magnetic field has only one component in the azimuthal direction, B_θ. Let (r, z, θ) be the standard cylinder coordinates, the Maxwell's system of equations is thus reduced into a single equation involving the magnetic field:

$$\frac{\partial B_\theta}{\partial t} + \left[\frac{\partial}{\partial z}\left(\frac{1}{\sigma\mu_0}\frac{\partial B_\theta}{\partial z}\right) + \frac{\partial}{\partial r}\left(\frac{1}{r\sigma\mu_0}\frac{\partial (rB_\theta)}{\partial r}\right)\right] = 0. \quad (1)$$

Here μ_0 and σ denote the magnetic permeability and electric conductivity, respectively. For the sinusoidal AC field, the magnetic field can be expressed using the phasor notation $B_\theta = \tilde{B}_\theta e^{i\omega t}$, where $\tilde{B}_\theta$ is a function of position (r, z) and $i^2 = 1$ and ω being the angular frequency. For time independent μ_0 and σ, the equation is given as:

$$\left[\frac{\partial}{\partial z}\left(\frac{\partial \tilde{B}_\theta}{\partial z}\right) + \frac{\partial}{\partial r}\left(\frac{1}{r}\frac{\partial \left(r\tilde{B}_\theta\right)}{\partial r}\right)\right] = i\omega\mu_0\sigma\tilde{B}_\theta + \frac{1}{\sigma}\tilde{\vec{j}} \times \vec{\nabla}\sigma, \quad (2)$$

Note that the last term on the right accounts for the change in direction of the electric current, j, when the electric current varies with temperature. This term should also not be neglected when multiphase phenomena or mold current are of interest.

After computing the real and imaginary components of the magnetic field, the electric current in the whole system can be obtained using the Ampere's law that is expressed as:

$$\tilde{\vec{j}} = \frac{1}{\mu_0}\left(\vec{\nabla} \times \tilde{B}_\theta\right). \quad (3)$$

Finally, the time average Lorentz force and Joule heating can be computed as:

$$\vec{F}_L = \mathrm{Re}\left(\frac{1}{2}\vec{j} \times \tilde{B}_{\theta\ Conjugate}\right) \quad (4)$$

$$Q_{Joule} = \mathrm{Re}\left(\frac{1}{2\sigma}\tilde{\vec{j}} \times \tilde{\vec{j}}_{Conjugate}\right) \quad (5)$$

3.1.2. Method Based on Magnetic Potential Vector

The second alternative is to use the $A - \phi$ formulation to calculate the electromagnetic field, where ϕ denotes the electric scalar potential and $\vec{A}$ is the magnetic vector potential. The electric scalar potential is obtained by solving the conservation equation of electric current:

$$\nabla \cdot \vec{j} = 0 \quad (6)$$

The treatment of current density, $\vec{j}$, includes two parts:

$$\vec{j} = -\sigma\nabla\phi - \sigma\frac{\partial\vec{A}}{\partial t} \tag{7}$$

The first term computed the imposed current as a function of electric conductivity of material, σ and electric scalar potential. The second term includes the effect of eddy currents generated in the process. Note that, the unsteady term in the right hand side of Equation 7 cannot be neglected in AC fields and in multiphase configurations even when a DC field is used.

The magnetic field is calculated by solving the equation of magnetic vector potential, that is, expressed as:

$$\nabla \times \left(\frac{1}{\mu_0}\nabla \times \vec{A}\right) = \vec{j} \tag{8}$$

$$\vec{B} = \nabla \times \vec{A} \tag{9}$$

Note that, to obtain a unique solution for Equation 8, the Coulomb gauge ($\nabla \cdot \vec{A} = 0$) is usually assumed. Finally, the Joule heating and Lorentz force are computed and added as source terms to the energy and momentum conservation equations, respectively.

$$Q_{Joule} = \frac{j^2}{2\sigma} \tag{10}$$

$$\vec{F}_L = \vec{j} \times \vec{B} \tag{11}$$

The boundary conditions using induction equation Equation 2 are simple and can be implemented at the internal or external interfaces of the mold. In opposite, expressing boundary conditions for the magnetic potential vector are not straightforward. They can be extracted by integration of Equation 9 and by imposing the axisymmetric version of the Ampere's law at a sufficiently large distance from the ingot axis. The drawback is the use of a larger calculation domain for the electromagnetic field than the one used for the thermal and momentum fields.

Thus, it is clear that the potential formulation is computationally more expensive compared to the common approach based on electromagnetic induction equation. However it can effectively model the current path including mold current and eddy current. In addition, it is very robust and accurate for solving the electromagnetic field in the presence of moving boundaries. Examples of calculation results are shown in **Figure 2**. The magnetic induction equation was the first method to be used.[56] The boundary conditions imposed at the mold did not allow the current to flow through the slag skin, as shown in Figure 2a. Using the vector potential-scalar potential formulation,[107] the distribution of electric current lines can be calculated in the entire domain including the mold, as shown in Figure 2b.

3.1.3. Proposed Models to Solve the Electromagnetic Field

Considering the conservation law of electric current in the slag, Medina et al.[62] solved the Laplace equation to establish Ohm's law in the slag where mold current was allowed. Patel[69,72] expressed the electric current distribution in the slag, electrode, and ingot in terms of a stream function to study effects of electrode/ingot size, applied AC frequency, and amplitude of current on magnetic and joule heating distributions. A parabolic relationship between the voltage drop and electrode diameter was predicted. In addition, Patel[85] presented an analytical solution in the form of Fourier-Bessel functions for distribution of current density in the slag, electrode, and ingot. Assuming an electrically insulating slag skin, a linear decrease in joule heating and voltage was found by the increase of the immersion depth. Li et al.[90] developed a three dimensional model based on the Finite Element Method (FEM) to study distributions of electric current, magnetic field, electromagnetic force, and Joule heat in the slag, electrode and ingot, where an electrically insulating slag skin was assumed. Hugo et al.[92] studied distributions of current density and joule heat in cases where mold current was allowed. Note that the electric current path is strongly dependent on operation parameters such as mold type, slag type, applied AC frequency, etc. In more recent works, electric current paths were calculated at different applied frequency and slag cap thickness for static or moveable molds including mold current.[107] More details on simulation of the mold current are given in the section dedicated to the modeling of the slag skin (section 4.1).

The first 3D simulation of ESR process was performed by Kharicha et al.[83] They simulated the electromagnetic field considering influences of the movement of slag-melt pool interface and dripping of droplets through the slag. Selected snapshots at different times of distribution of electric current density are shown in **Figure 3**. Note that, performing such "DNS" calculation is computationally very expensive. As such, no solidification and no melting could be included. It is generally advised to apply the robust 2D axisymmetric models for engineering applications.

3.2. Flow Field

The flow field is mainly driven by the Lorentz force and the thermal buoyancy in the slag. Typically, the flow pattern is a strong toroidal field, which efficiently promotes mixing of the liquid. Therefore, the temperature and compositional distributions are well homogenized inside the slag. However, the mixing is believed to be much weaker in the liquid melt pool, where both the electromagnetic and thermal buoyancy forces are much lower than in the slag. Nevertheless, recent 3D simulations[83] have shown the

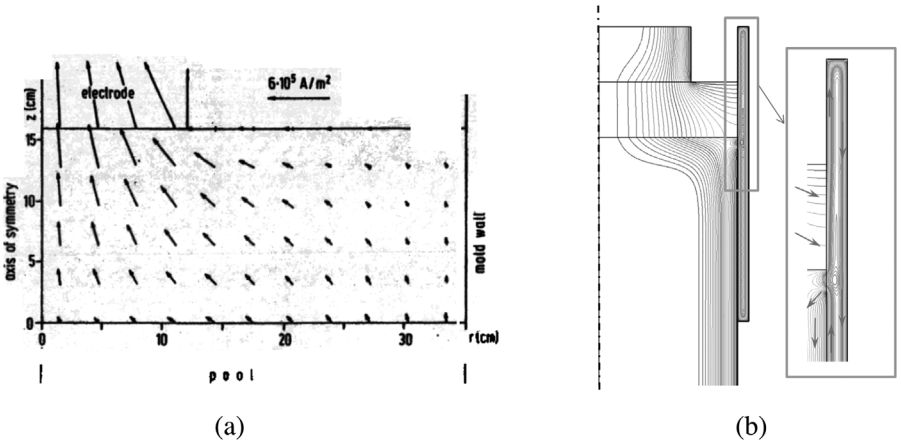

Figure 2. Modeling results of the distribution of electric current density are shown: a) in the slag and electrode using the magnetic induction formulation[56]; b) in the electrode, slag, ingot, and mold using the vector potential-scalar potential formulation.[107] Reproduced from refs.[56,107] with permission.

existence of a good mixing within the first centimeters under the slag/metal interface as a consequence of the impact of droplets and MHD wave development.

The first numerical model that accounted for the coupling of the flow and electromagnetic fields in the slag and melt pool was reported by Dilawari et al.[53] By neglecting thermal buoyancy, they predicted a linear relationship between the magnitudes of applied electric current and maximum velocity. **Figure 4**a shows the pioneering work of Dilawari et al. to compute the velocity field in the slag for a laboratory scale ESR process.[53] When the ingot diameter is small (<20 cm), the flow keeps a 2D nature (Figure 4b), as illustrated by the results of 3D simulations of Wang et. al.[108]

Kreyenberg et al.[56] investigated the flow under influences of the Lorentz and buoyancy forces in the ESR slag. It was shown that the buoyancy force could significantly alter the flow pattern. Jardy et al.[64] modeled the flow, electromagnetic and temperature fields in the slag. They predicted higher melt rate of the electrode when the buoyancy force is stronger than the Lorentz force.

Over the past decades, numerous models coupled with the flow field were proposed to study the influence of operational parameters such as ingot size, magnitude of applied current, applied AC frequency, and fill ratio (ratio between cross sections of the electrode and ingot) on the final quality of the ingot. Choudhary et al.[57] calculated the pool profile of the ingot where the coupling between

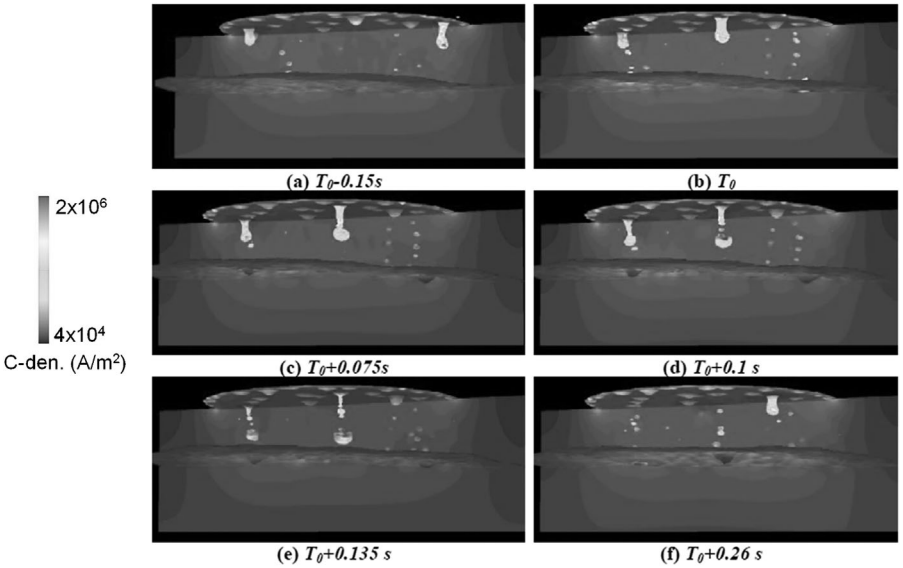

Figure 3. 3D simulation of the evolution of electric current density during formation and departure of droplets. Reproduced from ref.[83] with permission.

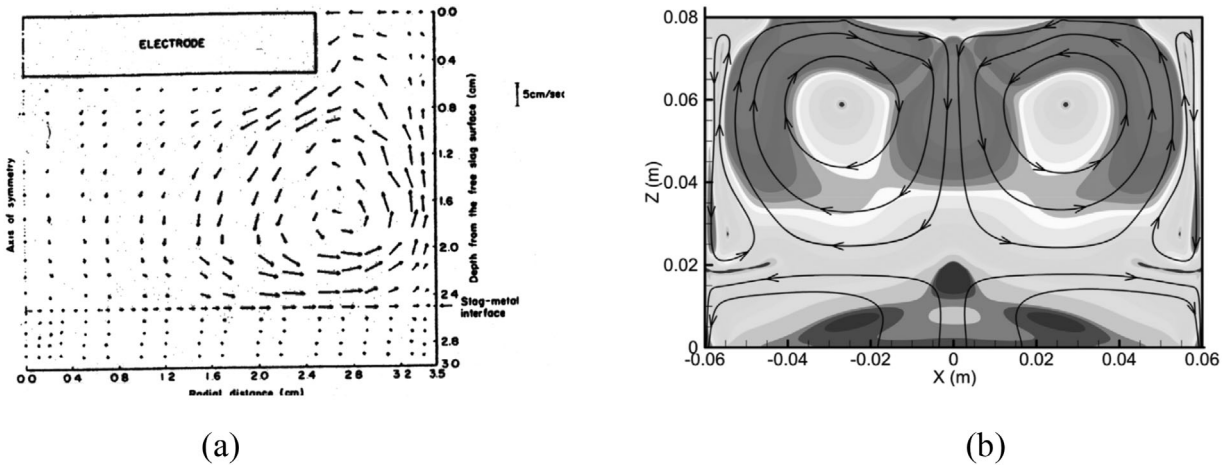

Figure 4. Simulated flow fields: a) the first published numerical results (2D) of the velocity field in slag and pool,[53] b) 3D flow streamlines and velocity magnitude (black 0, light gray 0.8 m s^{-1}), Alloy: AISI 201 stainless steel, Slag: CaF_2–Al_2O_3.[108] Reproduced from refs.[53,108] with permission.

turbulent flow, electromagnetic, and temperature fields in the slag was taken into account. The importance of fill ratio, the input power, and the immersion depth of electrode were addressed. Furthermore, they stated that the temperature field in the slag is more uniform at large-scale systems.[59] Ferng et al.[63] reported that the applied AC frequency could significantly influence the velocity field in the melt pool. However, a weak effect of AC mode compared to DC mode on the velocity field in the slag was predicted. Kharicha et al.[88] studied the importance of applied frequency on the shape of slag-pool interface, as well as variations in kinetic energy in the slag and melt pool. With the increase of applied frequency, the kinetic energy increases in both the slag and melt pool since larger displacement of the slag-pool interface was predicted at higher applied frequency. The importance of fluid flow is further discussed in the part dedicated to multiphase phenomena (section 4.2).

3.3. Heat Transfer and Solidification

The pool profile, local solidification time (LST) and subsequently microstructure of the ingot, melting of the electrode, mass transfer parameters, and thermodynamic information are governed by the thermal field. Maulvault[48] modeled the temperature field in an ingot to calculate the pool profile at quasi-steady state, where a so-called equivalent specific heat of alloy was used to treat the release of latent heat of fusion. Using a similar approach to model the temperature field in the ingot, Carvajal et al.[49] provided results for an Al–4.5Cu (wt%) alloy produced through ESR. Assuming a region of complete thermal mixing (uniform temperature) in the metal near slag-pool interface, an unsteady model was suggested by Basaran et al.[52] to calculate solidification parameters such as pool profile, depth of mushy zone, and solidification time. Considering slag to be at steady state and the growing ingot at an unsteady state, Ballantyne et al.[54] modeled temperature distribution in the ingot to calculate the related solidification parameters. Their results were successfully validated against experiments. Hugo et al.[109] have analyzed the influence of the mold current on the temperature and solid fraction field, as shown in **Figure 5**.

Attempts have been made to model segregation of alloy components including the thermal field and the hydrodynamic effects. Ridder et al.[55] introduced a combined theoretical-experimental study using a rather simple model to find a relationship between the pressure drop in the mushy zone (porous media), the interdendritic velocity, and the species concentrations. Results of experimental measurements for Ni–27Mo (wt%) and Sn–15Pb (wt%) alloys such as slag temperature or heat transfer coefficients were applied in the model. The solidus isotherm was considered as a moving boundary and no flow was modeled in the melt pool. Jeanfils et al.[58] calculated macrosegregation of multiple components in WASPALOY alloy using the Scheil model for solidification (no diffusion of components in the solid). The transient temperature field in an ESR ingot was calculated in which equivalent specific heat values were used to take into account the latent heat of fusion. The interdendritic flow in the mushy zone was estimated through the Darcy's law. Details of the model were presented by Mehrabian et al.[120]

Nastac et al.[65] proposed a stochastic model to predict the grain structure using the thermal history of a growing ESR/VAR ingot. Li et al.[97] used a coupled cellular automaton and the Finite Element Method (CAFE) to investigate the grain growth angle (GGA) of growing columnar grains. The tip velocity of the dendrites was calculated using the Kurz-Giovanola-Trivedi (KGT) model including tip and solutal undercooling.[121] Their

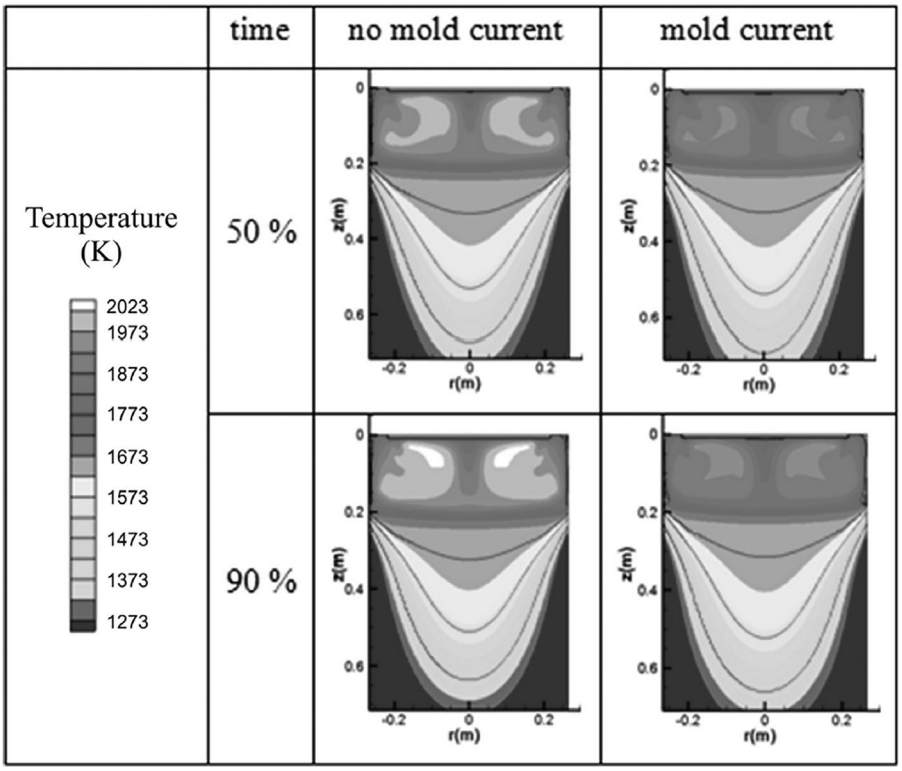

Figure 5. Temperature field in the slag bath and the ingot pool with and without mold current, at different remelting times including isolines of liquid fractions (0.01, 0.5, and 0.99). Reproduced from ref.[109] with permission.

calculated results were in good agreement with the experiment as shown in **Figure 6**. Rao et al.[95] used a multi-componential KGT model for the growth kinetic to study crystal morphology and GGA of a steel alloy. They observed a columnar-to-equiaxed transition (CET) after examining the ingot. Furthermore, they stated that GGA is smaller at lower melt rate.

The shrinkage of an ESR ingot and the subsequent formation of an air gap between mold and ingot strongly influences the cooling condition of the system. Sanchez Sarmiento et al.[60] calculated the temperature field for a Ni-based ingot considering a variable heat transfer coefficient at the ingot-mold interface to model the air gap expansion during ingot cooling. Yang et al.[70] introduced a thermal/elastic Finite Element based model to calculate stress during solidification of an Inconel 706™ alloy. For validation, the calculated surface temperature of the ingot was compared with experimental measurements. Eickhoff et al.[98] assumed a prescribed parabolic temperature distribution in the whole ingot. Then, radial contraction of solidifying ingot was calculated to estimate air gap thickness and length of full contact between ingot and mold. For a laboratory scale ESR ingot (≈200 mm), maximum values of 1.8 and 30 mm were calculated for the radial contraction and contact length, respectively.

The establishment of a relationship between the operational parameters and the thermal state of the electrode is of primary interest due to numerous chemical and electrochemical reactions occurring near the tip of the melting electrode. Mitchell et al.[50] calculated steady state temperature profile of the electrode. They predicted a large temperature gradient at the tip of the electrode that can certainly influence the reactivity of active chemical elements. Mendrykowski et al.[51] introduced a one dimensional model to compute the thermal field within the electrode. They found that heat radiation to the electrode is negligible compared to the heat conduction along the electrode. Tacke et al.[61] proposed an approximation formula for the immersion depth and the shape of the electrode tip. Furthermore, they investigated the influence of the operational parameters and the system size on the melting condition of the electrode. Their results were validated against experiments.

Viswanathan et al.[67] studied numerically and experimentally the relationship between melt rate, input power, and pool profile of the ingot. By increasing the melt rate, a linear increase in pool depth was reported. Kelkar et al.[68] presented details of an analysis of the turbulent flow, temperature, and magnetic fields for a Ni-based 718™ alloy produced by ESR. Furthermore, Rückert et al.[76] analyzed details of calculation results for the production of AISI304 ingots through ESR process. Their results were validated against experiments. Weber et al.[79] predicted that decreasing the filling ratio leads to an increase of both the melt rate of the electrode and the volume of the liquid pool. Patel et al.[80] used the commercial software

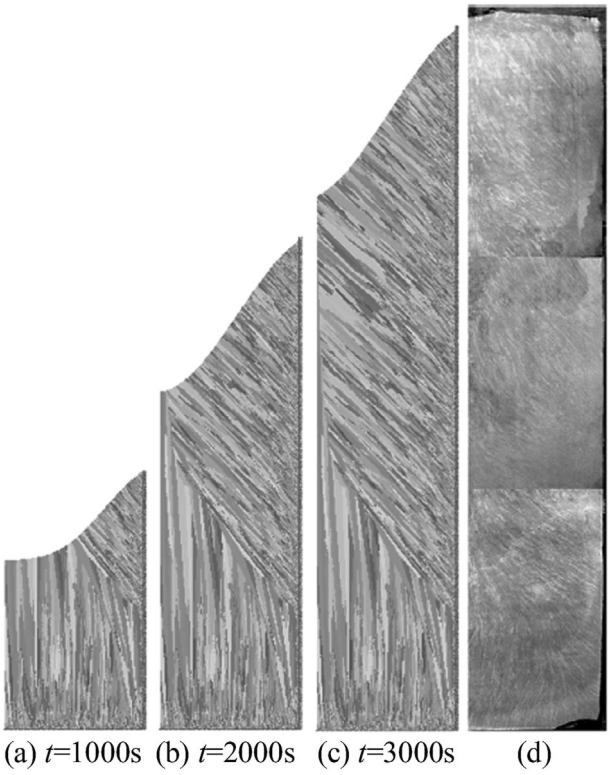

Figure 6. Comparison between numerical and experimental results of the microstructure evolution at the longitudinal section of an ESR ingot for different points in time for the alloy (H13 Die Steel). Reproduced from ref.[97] with permission.

(MeltFlow) to study the effect of filling ratio on pool depth for a 718™ and a 304™ stainless steel. Results regarding the heat loss through the slag-mold interface were analyzed. Furthermore, they predicted that increasing the filling ratio leads to a decrease of the pool depth of the ingot.

Assuming a constant thickness of the liquid metal film which forms at the tip of the electrode (≈8 mm), Yanke et al.[91] used heat transfer coefficients at the slag-electrode interface to predict the melt rate of the electrode for alloys Inconel 718™ and Waspaloy™. Furthermore, they studied effects of system size, applied current, and thickness of the slag skin layer on the melt rate and the pool depth.[99] Kelkar et al.[93] developed a transient model capable of predicting flow field, temperature field, magnetic field, pool shape, inclusion motion, Rayleigh number, and local solidification time (LST). Their modeling results were validated against experiments, as shown in **Figure 7**.

Wang et al.[96] proposed a three dimensional model for a laboratory scale ESR process to study the effect of applied current on the general system behavior. The calculated pool profile was validated against experiments. Yan-Wu et al.[71] estimated that the LST could be longer than 1 h at the ingot center (ϕ 950 mm), whereas the primary dendrites arm spacing is fairly small (≈140 μm). Their modeling results were compared with experimental measurements. Krane et al.[86] studied the influence of melt rate on crystal morphological parameters of Inconel 718™ alloy. Both primary and secondary dendrite arm spacing were found to increase with the increase of melt rate. Giesselmann et al.[104] developed a combined 2D axisymmetric and 3D model to study an ESR process for the production of alloy 718. Furthermore, they observed CET at the central region of ingot. They experimentally measured grain growth angle (GGA) and secondary dendrite arm spacing (≈120 μm).

Jardy et al.[78] stated that the probability of freckle formation in VAR or ESR can be related to the local Rayleigh number. Thus, an optimum melt rate to produce a high-grade ingot could be achieved when local Rayleigh numbers are kept at minimum values. In fact, the macrosegregation in an ingot is strongly governed by the flow in the melt pool and mushy zone.[105] Wang et al.[101] attempted to model macrosegregation of Ni in AISI 201 stainless steel for a laboratory scale ESR ingot (ϕ 120 mm). As shown in **Figure 8**, they observed negative segregation at the lower part and positive segregation in the upper part of the ingot. Their results were validated against an experiment in which the slag was composed of calcium fluoride, 75 mass pct., and aluminum oxide, 25 mass pct. The composition of Ni at the final ingot was analyzed using the method of Spectrolab™ optical emission spectrometer. Surprisingly, they observed a

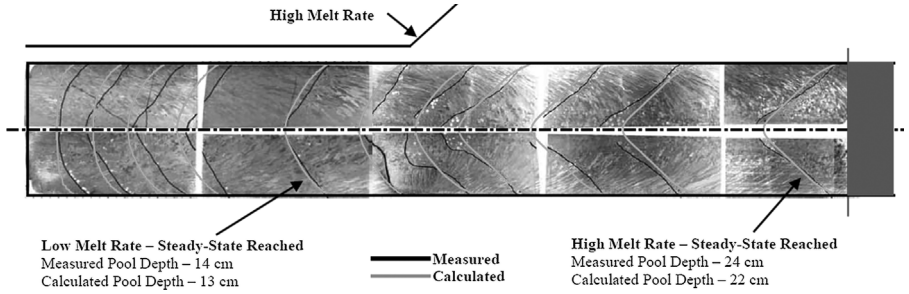

Figure 7. Comparison between the transient predicted and measured pool profile of an ingot for the Alloy 718. The slag composition is 70%CaF_2–15%CaO–15%Al_2O_3. Reproduced from ref.[93] with permission.

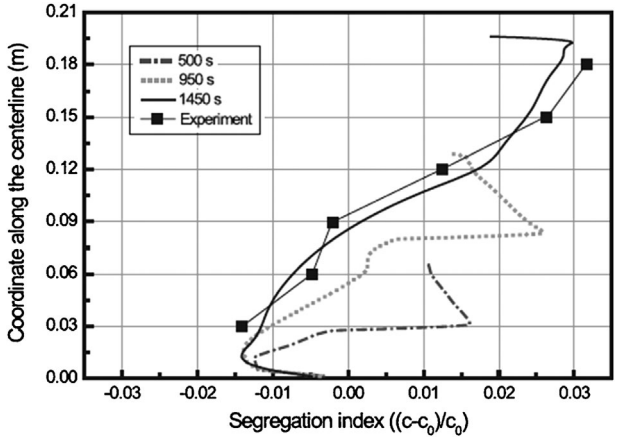

Figure 8. Numerical prediction compared with experiments of the evolution of segregation index along the centerline of a small size ESR ingot (AISI 201 stainless steel) at different remelting time (500–1450s). The slag is made of CaF_2 and Al_2O_3. Reproduced from ref.[101] with permission.

strong macrosegregation that might be due to melting of a dual alloy's electrode. Furthermore, macrosegregation of multiple components in Inconel 625™ alloy was studied by Fezi et al.[103] considering effects of mushy zone permeability, ingot diameter, initial composition of the electrode, and applied current.

4. Special Topics in the ESR Process

4.1. Prediction of the Slag Skin Thickness and the Mold Current

Proper modeling of the melting process depends on the ability of the model to predict the correct electric current pattern in the system, as it primarily controls the magnitude and the location, where the Joule heating is released. When the mold is electrically insulated from the baseplate, the ESR process experiences the apparition of arcs between the ingot and the mold, which can damage the surface of the mold. No arc appears when the mold is in electric contact with the baseplate (live mold). In industry these facts suggested that the current indeed able to cross the slag skin to enter the mold.

Depending on the geometry, the properties, and the mold type, the electric current selects the less resistive path through the slag, the mold, the ingot, and the baseplate. The mold current can greatly influence distributions of Lorentz force and Joule heating in the system.[105] To predict the amount of mold current, the most important parameter is the electrical conductivity of the slag. This parameter increases strongly in magnitude with increasing temperature, so the slag is much more conducting in its liquid phase than in its solid phase. The amount of mold current is directly controlled by the ratio of liquid to solid electrical conductivities. As previously mentioned, the electric conductivity of the solidified slag skin layer is not well-known, but the mechanism of current conduction through the solidified slag layer is stated to be ionic.[122] However, the types of faradaic reactions and involved ions are unknown.

Predicting numerically the amount of mold current is difficult, this is why most of simulations found in literature use the hypothesis of perfectly isolated mold which has also the advantage to simplify considerably the formulation of the electromagnetic boundary conditions at the mold. The model developed by Patel[69] accounts for the mold currents by simply directing a predefined part (20%) of the total current toward the mold. As such, this model is simple but is not able to predict the exact proportion of the mold to the total current.

The effects of the slag skin on the electromagnetic and thermal field were modeled in two different ways. The first is a direct simulation of its thickness.[75,79,109,117] The solidification of the slag is simulated in the same ways, as the metal alloy in the pool using the liquidus and solidus temperature as input. This choice requires the use of sufficiently small volume elements near the mold in order to resolve the variation of solid fraction. The second way is to simulate implicitly its effects simply applying a thermal and electrical resistance at the slag mold interface.[68,94] The validity of this approach is supported by the fact that the slag skin is usually very thin ($\approx$1 mm), so that the thermal and electric fluxes can be considered as perpendicular to the mold surface. Applying this method is recommended for industrial application as only the size of the slag skin must be estimated. A one-dimensional equation for the transport of the skin thickness along the mold can be easily be extracted by integrating the enthalpy equation through its thickness (δ)[94]:

Using the two aforementioned methods, many recent works have shown that the resistance of the solid slag layer is indeed not high enough to prevent the current to enter the mold.[94,109,105,114,117] Assuming an electrically insulator slag skin, Weber et al.[79] have shown that the difference between the slag liquidus and alloy liquidus temperatures is a critical parameter to determine the thermal field in the entire ESR process. Yanke et al.[99] used the Volume of Fluid (VOF) method to track the slag/metal interface and so allowing simulation of slag freezing to the mold (**Figure 9**). They also neglected the possibility for the current to cross the slag skin. Through its sole thermal effects, the slag skin thickness is found to have a significant impact on the melt rate and depth of metal pool.

Kharicha et al.[75,94] have considered the influence of mold currents on the process. Considering a sufficiently low electrical conductivity for the skin, the thickness of skin was found to be thinner at the level of the slag/air interface compare to the level of the slag/metal interface. These results explain why often during ESR processes there are two peaks in the heat fluxes measured at the mold. The electric current path can strongly influence the conditions

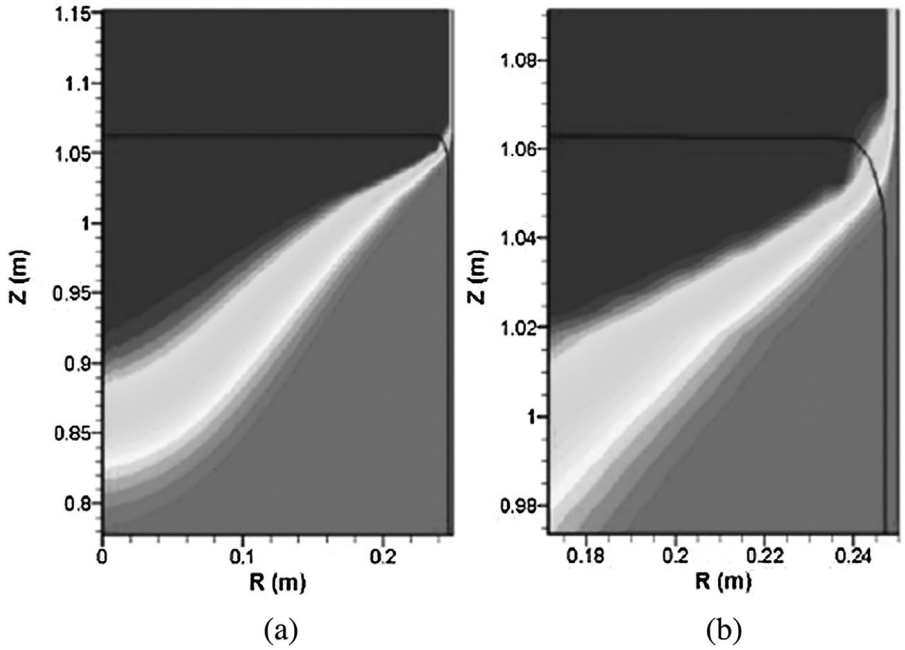

Figure 9. Prediction of the solidification and the slag/metal boundary during an ESR process. The color indicates the solid fraction (black 0, gray 1), the boundary between slag and metal phases is represented by the black line; b) is the close up near the mold wall. The simulation is performed for alloy 718 considering the following composition for the slag: 70%CaF_2–15%CaO–15%Al_2O_3. Reproduced from ref.[99] with permission.

for flow and solidification. Kharicha et al.[66] reported the importance of mold current on the shape of slag-pool interface and the distribution of Lorentz force. Furthermore, they pointed out the relationship between slag skin thickness, temperature fluctuation in the slag, and the amount of mold current.[75,77] Increasing the amount of mold current may lead to decreasing the thickness of the slag skin. Additionally, the electrode immersion depth can affect both the thickness of slag skin and the amount of mold current.[94] Assuming an electrically insulating slag skin, the total heat generated in the slag region was found to be much higher than that really generated during the process.[75,105] The total electrical resistance of the system and consequently the amount of generated power decreases because of the mold current that is further described in ref.[94] The most important finding is that the slag skin together with the mold current has determining effects on the internal as well as surface quality of the final ingot.[105,109,114]

To act as an electrical insulator, the solidified slag layer must be at least 1000 times more resistive than the slag at the liquid state.[105] To conclude, it is clear that the assumption that the electric current cannot cross the solidified slag layer must be used with extreme care.[105,109,114,117]

4.2. Multiphase Aspects

The ESR process involves two liquids, liquid steel and liquid slag. From a fluid dynamic point of view, the ESR process is clearly a multiphase process including a free interface (liquid metal/liquid slag = slag/pool) and a mixed area (slag and falling metallic droplets). In 2D "single phase" simulations, the presence of droplets is handled through their effect on the enthalpy and momentum conservation equation. Droplets are believed to be the main actor in the transport of heat from the slag to the liquid pool. The slag/pool interface has been assumed flat and quiescent.

It is obvious that the slag-pool interface movement as well as the formation, departure, and dripping of droplets through the slag could significantly influence the hydrodynamic conditions of the process.[74] The pool depth is predicted to be deeper when the slag-pool interface is allowed to move.[82] Additionally, effects of the size of the droplets on the global electromagnetic, flow, and temperature fields in the slag were analyzed.[73] Kharicha et al. proposed a multiphase model to estimate the volume-averaged impact of droplets in the slag and in the melt pool.[81] Considering the complex interaction between flow, temperature, and magnetic fields, Kharicha et al.[83] performed a 3D calculation to study the chaotic flow in the slag and the melt pool during formation and dripping of droplets. The impact of the interfacial energy between slag and metal melt on the size of droplets and consequently on the portion of the electrical resistance swing in the slag were also addressed.[87] The magnitude of the interfacial tension is highly affected by temperature and electrochemical reactions. Small interfacial tension leads to the formation of small droplets at the electrode tip. Wang

et al.[102] developed a full scale 3D model including solidification assuming a parabolic shape for the tip of the electrode. They calculated the residence time of droplets in the slag and compared their results with empirical models. Unfortunately, all these aforementioned 3D "direct numerical simulations" are still very expensive in term of computational time and should be reserved to detailed investigations. The reason is the large difference between the time scales related to multiphase phenomena ($\approx 10^{-3}$) and those related to heat transfer in the liquid pool ($\approx 10^{3}$ s). However, the 3D multiphase results are of great benefit for the tuning and adaptation of a 2D model dedicated to fast calculation of industrial processes. One of the most important finding is that the presence of droplets disturbs the distribution of the electric current density. This induces an additional Joule heating generation just under the electrode. The droplets generate strong turbulences in the slag during dripping. When the applied electric current is sufficiently high, waves are generated at the liquid pool interface. These waves contribute likely to the ingot surface quality.[110,113,116]

4.3. Melting and Shape of the Electrode

Predicting the melt rate of the electrode is one of the major challenges in the simulation of the ESR process. The first difficulty is the poorly known thermal conductivity of the slag as a function of both composition and temperature. The second is the contribution of the turbulence to the heat advection and conduction just under the electrode. The third is the estimation of the liquid film thickness dependent on both the melting rate and the flow conditions. The thermal state and melt rate of the electrode are considerably influenced by the flow in the slag. The MHD makes the melt rate, the immersion depth, and the shape of electrode tip to be interdependent parameters. Kharicha et al.[84,100] studied melting of the electrode tip using the multiphase Volume of Fluid (VOF) method. The importance of electrode feeding velocity, immersion depth, shape of the electrode tip, and release of Joule heat were addressed. They stated that melting of electrode is an unstable process, and thus the immersion depth of the electrode must be controlled to achieve steady state melting.

Recently, Kharicha et al.[100] found that coupling between the Joule heat release and the melting rate is very unstable. Furthermore, it was shown that the stability in simulation can be achieved only by including a numerical adaptation on immersion depth and feeding velocity of electrode. Within the framework of the multiphase model, details of process conditions such as temperatures, velocities, and magnetic forces can be captured. However, the multiphase method used in this investigation is computationally expensive. Therefore, Karimi-Sibaki et al. combined a single phase approach with a Stefan model to predict the electrode shape.[106] To avoid the Joule heating-melting instability, a numerical adaptation of electrode position in the slag has been implemented in order to achieve steady state melting. The generated power in the system was found to be dependent on both immersion depth and shape of electrode tip. It was observed that the shape of electrode tip is very similar for systems running with the same ratio of the power generation to melt rate. Furthermore, the fully coupled model predicted that the melt rate, immersion depth, and shape of electrode tip are interdependent parameters of the process, as shown in **Figure 10**. However, all the aforementioned investigations were performed on small laboratory scales ESR processes. Similar shapes could be possibly achieved with an industrial scale electrode, but the immersion depth must be much larger than in usual practice. However the flow pattern, which affects the heat flux entering the electrode, varies strongly with the scale of the process. For small scales electrode, the slag flow is almost fully driven by the Lorentz force. For higher scales and fill ratio, the bulk slag flow is mostly driven by thermal buoyancy, the Lorentz force dominates only near the electrode extremity. So for higher immersion depth, it could be expected a conical frustum tip electrode shape.

4.4. Non-Metallic Inclusions (NMI)

Here, features of species transport as a major phenomenon occurring in the ESR are briefly discussed. Different contributions to species transport are easily recognized in removal and precipitation of non-metallic inclusions in the slag and melt pool, chemical and electrochemical reactions in the slag, and refinement of the alloy through the process.

Chemical reactions taking place within the slag bath or at metal-slag interfaces dominantly influence type of inclusions in the ingot as reported by Mitchell.[123] It was stated that nucleation and growth of inclusions in the ingot might occur, which can be avoided by adding more deoxidants to the melt pool. Furthermore, a careful selection of the composition of slag is essential to increase residence time of droplets inside the slag bath.[124] Kay et al.[125] proposed possible mechanisms of inclusion removal including floatation, absorption, and chemical reaction. They stated that a deep melt pool could efficiently enhance flotation of inclusions. The floating inclusions in the melt pool are absorbed at slag-pool interface. Furthermore, inclusions could be dissolved at high temperature as a consequence of chemical reactions in the slag (e.g., reactions of silicon oxide and aluminum oxide). Since inclusions coming from the electrode are either mechanically removed or dissolved, the inclusion content of ESR ingots are believed to be mainly generated by precipitation and growth processes in the liquid metal pool, as well as the mushy region. Experimental analyses have shown that the number density of the inclusions decreases from the outer surface toward the ingot center while their size

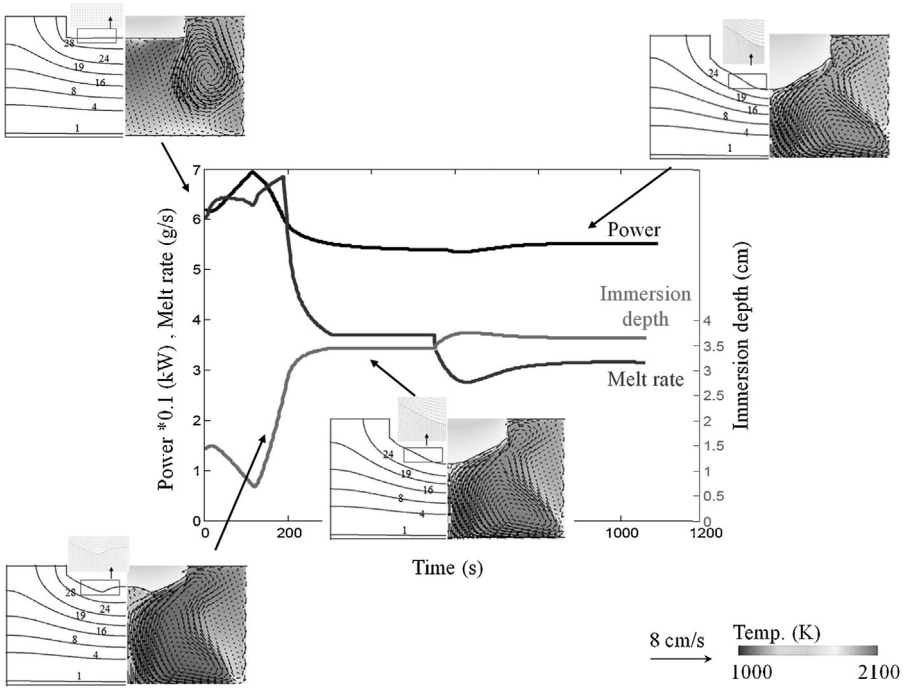

Figure 10. Simulated results that demonstrate the dependence of an experimental size electrode tip shape during melting on parameters such as power, melt rate, and immersion depth. The slag is made of 40%CaF_2–30%CaO–30%Al_2O_3. Snapshots at different times are shown for flow, temperature, and electric potential fields. Reproduced from ref.[116] with permission.

increases. Simulations were performed to explore the origin of this segregation. Kharicha et al.[89] modeled the nucleation and the transport of the NMI in the liquid pool. Assuming that the inclusions nucleate uniformly between the lines 0.01 and 0.1 solid fractions within the mushy region, they found a radial distribution of NMI in the ingot. The segregation in radial direction was found to be stronger for larger inclusions as shown in **Figure 11**.

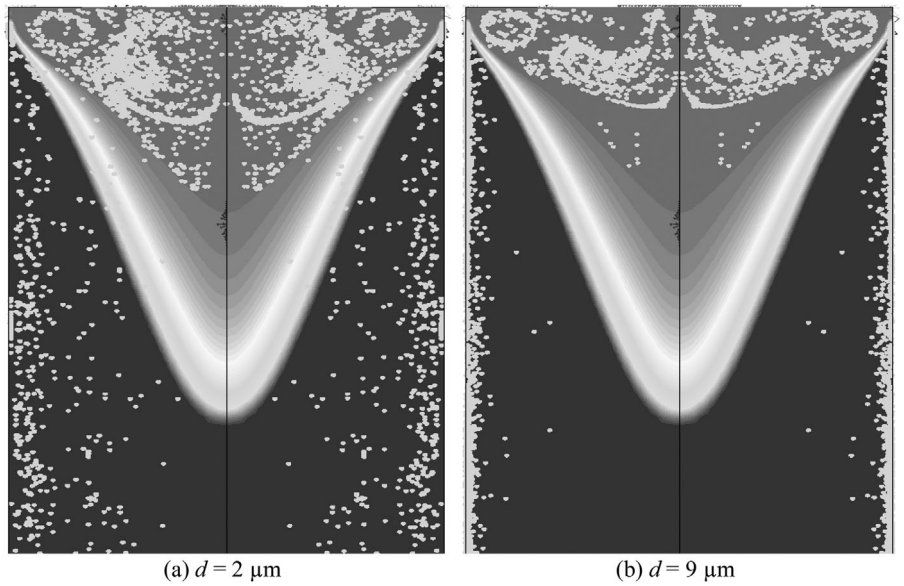

Figure 11. Distribution of inclusions (white dots) in the solidifying ingot for different inclusion diameters. The background color represents the liquid fraction (black 0, gray 1). The alloy is steel grade X12CrNiMoV12-3, and the slag is made of CaF_2–CaO–Al_2O_3. Reproduced from ref.[89] with permission.

4.5. Chemical and Electrochemical Reactions

Numerous chemical and electrochemical reactions can be carried out in the slag.[17,18] Reactions are majorly taking place within the slag bath or at slag-metal-gas-mold interfaces.[5] Aluminum–silicon oxides and Sulfur are frequently reacting. A mechanism including a series of electrochemical reactions was postulated for Sulfur removal during ESR. Minh et al.[126] melted a copper electrode in similar conditions as typical for a ESR process. They suggested a diffusion controlled electrochemical reaction for the Sulfur. Kato et al.[127] studied behavior of oxygen and Sulfur during DC melting of electrode during ESR. They observed that concentrations of Sulfur and oxygen in the final ingot are very dependent on the electrode polarity during remelting. A higher amount of oxygen and lower amount of Sulfur was traced in the ingot produced through the ESR with the negative polarity of the electrode.

The pioneering work of Kawakami et al.[128,129] described possible electrochemical reactions occurring at the tip of electrode. They observed that the melt rate of the electrode is dependent on the electrode polarity in DC ESR processes. Mitchell et al.[130] pointed out further possible electrochemical reactions after performing a series of experiments to measure electrochemical polarization overpotential. They used the well-known Galvanostatic Pulsing technique to measure magnitudes of overpotential resulting from concentration polarization at the interface between iron and CaF2-based slags. A significant change in composition of a pure iron electrode was observed after polarization. A noticeable increase in composition of oxygen in the bulk of the electrode was measured using methods of optical and electron microprobe scans.

A loss of alloy elements such as Ti and Al due to electrochemical oxidation was reported as a significant issue during DC operation of ESR processes.[131] Reactions of special alloy elements such as Fe or Mn were also studied. Nowack et al.[132] postulated a relationship between current density (DC or AC) and potential. With the increase of the iron oxide content in the slag or the applied frequency, the overpotential decreases. Prange et al.[133] measured the magnitude of exchange current density at 1450 °C for an iron electrode immersed into the slag. Furthermore, Schwerdtfeger et al.[134] presented modeling results of curve fittings to describe an electrochemical mechanism of oxidation of titanium and aluminum, where iron oxide was considered as the major oxidizing agent for both of those elements. The reaction kinetics of Mn and Fe were analyzed by Fraser et al.[135] aiming to find the relevant mass transfer coefficients. They extended their investigation to examine the impact of the applied frequency and used mold type (isolated or live) on the reaction kinetics of Mn. They concluded that experimental results support a faradaic reaction of Mn on the interfaces of the slag-metal or slag-mold.[135,136]

It must be stated that modeling species transport during ESR is still in a very preliminary stage. Extensive dedicated efforts are required to develop high fidelity models considering the coupling between flow, heat, electromagnetic, and species concentration fields. Electrically resistive CaF_2-based slags are widely used in the electroslag remelting process to generate Joule heat for the melting of the electrode. Classically, the slag is modeled as an Ohmic conductor. This hypothesis is known to be valid only in the bulk slag and at very high electric current frequency (>1000 Hz). For conventional frequencies (0.2–50 Hz) and at the vicinity of metallic interfaces, it is necessary to

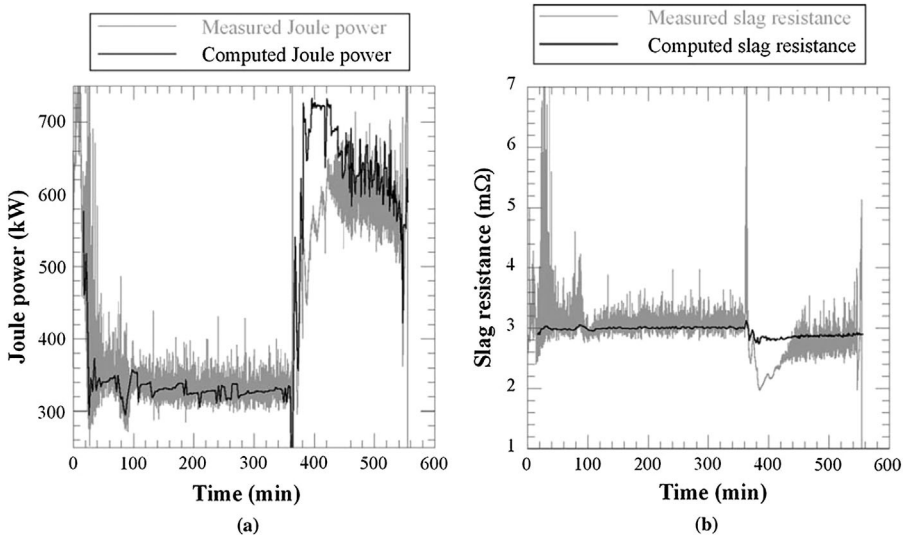

Figure 12. Computed and measured evolution of a) total Joule power, and b) slag resistance with time during remelting of a Ni-based alloy. Reproduced from ref.[79] with permission.

consider the relative movement of ions such as Ca^{+2}, F^{-}, Al^{3+}, or O^{2-}. As such, it is necessary to establish electrochemical models to study the electrical behavior of the slag. Karimi-Sibaki et al.[137–139] solved the dimensionless Poisson-Nernst-Planck (PNP) equations to model electro-migration and diffusion of ions. Spatial variations of concentrations of ions, charge density, and electric potential across the electrolyte are analyzed. They found that the anodic potential drop near the electrode is significantly larger than the cathodic potential drop in fully dissociated CaF_2–FeO slags. The aforementioned phenomenon is directly related to the concentration overpotential.[138,139]

5. Conclusion and Outlook

Modeling ESR as one of the most complex metallurgical processes is very challenging due to the strong level of coupling between MHD, thermal, and chemistry phenomena.

Thanks to the development in computational capacity, details about the droplet formation, as well as the MHD flows are now better understood. Because of the rise of new numerical models, many coupling mechanisms were discovered. Most of these mechanism are related to the electric current distribution: (i) The mold current is coupled to the slag flow and temperature, (ii) the melt rate, immersion depth, and shape of electrode tip are interdependent parameters of the process, which explain why (iii) the ingot surface quality is so related to electrode immersion depth. The years 1999–2016 have seen the rise of several models dedicated to the prediction of the chemical and structural composition of the final ingot. These models perform relatively well when the operating conditions (melt rate, applied current) are steady, however their performances are much lower in unsteady conditions.

Although large progress have been made in the last 20 years, a 3D simulation of industrial scale processes including all the Multiphysics will probably remain a dream even for the next 20 years. Physical properties of the liquid slag are one of the bottle necks. Direct numerical simulations must be used in order to continue the exploration of the multiphase aspects. Meanwhile, it is required to further develop volume-averaged models which enable us to estimate the occurring melting and solidification process.

Distribution, type, and size of inclusions in the final ingot are of great interest for industry. It is necessary to establish advanced models to include chemical and electrochemical reactions at interfaces, nucleating, and growth of inclusions, as well as their transport due to the MHD governed flows. Future model must enable us to investigate the influence of operational parameters such as applied AC frequency or the impact the slag composition might have on the characteristics of the final ingot.

If the heart of the ESR process is the liquid slag, its lung can be represented by the solidified slag skin. Knowing the electrical conductivity of the slag as function of temperature, an ideal model would predict how the voltage (or resistance) generated in the slag varies with the applied current and the electrode immersion depth. Examples of such predictions can be found in refs.[79,94,106] As shown in **Figure 12** however, in comparison with the measurements, the change in resistance with the increase of the applied current is underestimated by the model of Weber et al.[79] Perhaps the reason is related to the fact that the control system has suddenly "adjusted" the immersion depth. Due to the continuous intervention of the control system, the experimental data can hardly be used to validate a model. In other words, experiments performed in industrial plants should be carefully planned. In an ideal situation to validate the model, the control system should be temporally switched off.

It is necessary to take into account the effects of the mold current on the newly formed slag skin at the mold as the electrode penetrates into the slag. As time proceeds, the change of the electrode tip shape will induce an additional change in the electric resistance. The problem resistance-electrode immersion is one of the main tasks which should be tackled by future models. That is why none of the reviewed models can predict accurately the melting and the shape of the electrode. To achieve this goal, future models must imperatively take into account the way the electrode immersion is controlled during the process.

Coming back to the solidification in the liquid pool, investigation on the probability of the formation of macrosegregation or gas evolution during ESR requires further attention.[140] The proposed models to calculate macrosegregation during ESR are rather simple because of the use of the so-called enthalpy-porosity model of solidification.[101,103] The interdendritic velocity that dominantly influences the formation of macrosegregation in the ingot cannot be accurately modeled using simply permeability laws.[111] In the future, applying volume-averaged models such as two-phase, three-phase or five-phase models to predict growth of columnar or equiaxed dendrites can give us valuable insight into segregation phenomena in the ESR ingot.[141–144] For example, the columnar-to-equiaxed transition (CET) phenomenon that was commonly observed in production of Ni-based alloys through ESR needs further investigation.

The shrinkage of the ingot during solidification and formation of an air gap between ingot and mold have a significant effect on the efficiency of the mold cooling system, and consequently on the internal and surface quality of the final product. It is crucial to develop an accurate coupled model considering interactions between solidification, electric current distributions and ingot shrinkage.

Finally, the proposed species transport models to describe the involved chemical and electrochemical

reactions are not complete. It is essential to develop species transport models coupled with MHD phenomena in order to understand the role of the operational parameters on the efficiency of purification in the ESR process.

Acknowledgements

The authors acknowledge the financial support by the Austrian Federal Ministry of Economy, Family and Youth and the National Foundation for Research, Technology and Development within the framework of the Christian Doppler Laboratory for Advanced Process Simulation of Solidification and Melting.

Received: March 15, 2017; Revised: June 27, 2017; Published online: August 14, 2017

Keywords: electrochemistry; electroslag; Joule heating; macrosegregation; magnetohydrodynamics; melting; modeling; remelting; simulation; slag; solidification

References

[1] N. G. Slavyanov, *Electrical Metal Casting*, SPB, **1892**.
[2] W. E. Duckworth, G. Hoyle, *Electro-Slag Refining*, Chapman and Hall publisher, London, United Kingdom **1969**.
[3] P. A. E. Armstrong, *U.S. Patent No. 1,781,490*, **1930**.
[4] W. A. McKeen, L. G. Joseph, D. M. Speher, *Met. Prog.* **1962**, *82*, 86.
[5] G. Hoyle, *Electroslag Processes*, Applied Science Publishers, London, United Kingdom **1983**.
[6] R. H. Nafziger, *The Electroslag Melting Process*, U.S. Bureau of Mines, Washington, USA **1976**.
[7] B. I. Medovar, G. A. Boyko, *Electroslag Technology*, Springer-Verlag publisher **1991**.
[8] G. Hoyle, in: *6th Int. Vac. Metall. Conf. on Special Melting*, San Diego **1979**, p. 624.
[9] E. J. Pickering, *ISIJ Int.* **2013**, *53*, 935.
[10] A. Mitchell, *Electroslag and Vacuum Arc Remelting Processes*, AIME, Iron and Steel Society **1985**.
[11] K. O. Yu, J. A. Domingue, G. E. Maurer, H. D. Flanders, *JOM* **1986**, *38*, 46.
[12] S. Kou, *Ph.D. Thesis*, MIT, **1978**.
[13] Y. M. Shash, T. E. Gammal, M. A. El Salamoni, F. A. Denkhaus, *Steel Res.* **1988**, *59*, 269.
[14] A. Mitchell, R. M. Smailer, *Int. Met. Rev.* **1979**, *5–6*, 231.
[15] J. M. Sathaye, *M. Sc. Thesis*, UBC, **1977**.
[16] H. Holzgruber, *PhD Thesis*, MU Leoben, **2005**.
[17] M. E. Peover, *J. Inst. Met.* **1972**, *100*, 97.
[18] A. Mitchell, *Can. Metall. Q.* **1981**, *20*, 101.
[19] M. Allibert, H. Gaye, J. Geiseler, D. Janke, B. J. Keene, D. Kirner, M. Kowalski, J. Lehmann, K. C. Mills, D. Neuschütz, R. Parra, C. Saint-Jours, P. J. Spencer, M. Susa, M. Tmar, E. Woermann, *Slag Atlas*, Verlag Stahleisen GmbH, Düsseldorf, Germany **1995**.
[20] W. W. Smeltzer, Z. A. Foroulis, *Metal-Slag-Gas Reactions and Processes*, Electrochemical Society Publisher, Princeton, USA **1975**.
[21] M. Etienne, *PhD Thesis*, UBC, **1971**.
[22] G. Patlesky, H. Blele, H. J. Flelscher, *J. Vac. Sci. Techol.* **1972**, *9*, 1318.
[23] M. Allibert, J. F. Wadier, A. Mitchell, *Ironmaking Steelmaking* **1978**, *5*, 211.
[24] A. Mitchell, M. Hilborn, E. Samuelsson, A. Kanagawa, *Superalloy*, TMS, **1988**, 407.
[25] C. B. Shi, J. Li, J. W. Cho, F. Jiang, I. H. Jung, *Metall. Mater. Trans. B* **2015**, *46*, p. 2110.
[26] K. C. Mills, B. J. Keene, *Int. Met. Rev.* **1981**, *1*, 21.
[27] L. Zheng, B. Zhu, *Electroslag Metallurgy Theory and Practice (in Chinese)*, Metallurgical Industry Publisher, Beijing **2011**.
[28] J. Korp, R. Rabitsch, R. Schneider, in *Liquid Metal Processing and Casting (LMPC)*, ASM International, Santa Fe **2005**.
[29] J. Korp, *PhD Thesis*, MULeoben, **2007**.
[30] M. Hajduk, T. E. Gammal, *Stahl und Eisen* **1979**, *99*, 113.
[31] T. E. Gammal, M. Hajduk, *Arch. Eisenhüttenwes* **1978**, *49*, 235.
[32] B. Birol, G. Polat, M. Saridede, *JOM* **2015**, *67*, 427.
[33] R. Taylor, K. C. Mills, *Arch. Eisenhüttenwes* **1982**, *53*, 55.
[34] A. Mitchell, J. F. Wadier, *Can. Metall. Q.* **1981**, *20*, 373.
[35] X. Li, S. Wang, J. Zhao, Y. Cui, Y. Chen, *Adv. Mater. Res.* **2011**, *239–242*, 1960.
[36] F. Liu, Z. Jiang, X. Zang, X. Geng, in *Liquid Metal Processing and Casting (LMPC)*, TMS, Santa Fe **2009**, p. 213.
[37] K. Wroblewski, B. Dibiaso, J. Fraley, J. Fields, S. Rudoler, in *Liquid Metal Processing and Casting (LMPC)*, Wiley, Austin **2013**, p. 43.
[38] S. Akbari, J. Reitz, B. Friedrich, in *Liquid Metal Processing and Casting (LMPC)*, Santa Fe **2009**, p. 243.
[39] A. Mitchell, S. Joshi, *Metall. Trans.* **1972**, *3*, 2306.
[40] K. Ogino and S. Hara, *Density, Surface Tension and Electrical Conductivity of Calcium Fluoride Based Fluxes for Electroslag Remelting (in Japanese)*, UDC **1977**.
[41] D. Gohil, K. C. Mills, *Arch. Eisenhüttenwes* **1981**, *52*, 335.
[42] B. V. Muu, *Untersuchung der Grenzflächenspannung zwischen Schlacken des systems CaO- CaF_2-Al_2O_3* und Stahlschmelzen aus 100Cr6 und X85WmoCo6.5.5, Neue Hütte, Heft *6* **1976**, p. 335.
[43] B. J. Keene, K. C. Mills, *Arch. Eisenhüttenwes* **1981**, *52*, 311.

[44] K. C. Mills, L. Yuan, R. T. Jones, *J. South Afr. Inst. Min. Metall.* **2011**, *111*, 649.
[45] A. Plotkowski, J. de Barbadillo, M. J. M. Krane, *Mater. Sci. Techol.* **2016**, *32*, 1249.
[46] L. Willner, P. Varhegyi, *Arch. Eisenhüttenwes* **1976**, *47*, 205.
[47] B. Hernandez-Morales, A. Mitchell, *Ironmaking Steelmaking* **1999**, *26*, 423.
[48] M. A. Maulvault, *PhD Thesis*, MIT, **1967**.
[49] L. F. Carvajal, G. E. Geiger, *Metall. Trans.* **1971**, *2*, 2087.
[50] A. Mitchell, S. Joshi, J. Cameron, *Metall. Trans.* **1971**, *2*, 561.
[51] J. Mendrykowski, J. J. Poveromo, J. Szekely, A. Mitchell, *Metall. Trans.* **1972**, *4*, 1761.
[52] M. Basaran, R. Mehrabian, T. Z. Kattamis, M. C. Flemings, *A Study of the Heat and Fluid Flow in Electroslag Remelting, Report CTR 74–36,* Army Materials and Mechanics Research Center, USA **1974**.
[53] A. H. Dilawari, J. Szekely, *Metall. Trans. B* **1977**, *8*, 227.
[54] A. S. Ballantyne, A. Mitchell, *Ironmaking Steelmaking* **1977**, *4*, 222.
[55] S. D. Ridder, F. C. Reyes, S. Chakravarty, R. Mehrabian, J. D. Nauman, J. H. Chen, H. J. Klein, *Metall. Trans. B* **1978**, *9*, 415.
[56] J. Kreyenberg, K. Schwerdtfeger, *Arch. Eisenhüttenwes* **1979**, *50*, 1.
[57] M. Choudhary, J. Szekely, *Metall. Trans. B* **1980**, *11*, 439.
[58] C. L. Jeanfils, J. H. Chen, H. J. Klein, *Superalloys* (Eds: Tien et. al.,), ASM, Metals Park, OH **1980**, 119.
[59] M. Choudhary, J. Szekely, *Ironmaking Steelmaking* **1981**, *5*, 225.
[60] G. S. Sarmiento, E. Vicente, A. Leyt, in *2nd Int. Conf. on Numerical Methods in Thermal Problems*, Venice, **1981**, p. 697.
[61] K. H. Tacke, K. Schwerdtfeger, *Arch. Eisenhüttenwesen* **1981**, *52*, 137.
[62] S. F. Medina, P. de Andres, *Ironmaking Steelmaking* **1987**, *14*, 110.
[63] Y. M. Ferng, C. C. Chieng, C. Pan, *Numer. Heat Trans. A* **1989**, *16*, 429.
[64] A. Jardy, D. Ablitzer, J. F. Wadier, *Metall. Trans. B* **1991**, *22*, 111.
[65] L. Nastac, S. Sundarraj, K.-O. Yu, *Superalloys 718,625,706 and Various Derivatives* (Ed: E. A. Loria), TMS Publisher, USA **1997**, p. 55.
[66] A. Kharicha, A. Ludwig, M. Wu, *Mater. Sci. Eng. A* **2005**, *413–414*, 129.
[67] S. Viswanathan, D. K. Melgaard, A. D. Patel, D. G. Evans, in *Liquid Metal Processing and Casting (LMPC)*, ASM International, Santa Fe **2005**.
[68] K. M. Kelkar, S. V. Patankar, A. Mitchell, in *Liquid Metal Processing and Casting (LMPC)*, ASM International, Santa Fe **2005**.
[69] A. D. Patel, in *Liquid Metal Processing and Casting (LMPC)*, ASM International, Santa Fe **2005**.
[70] W. Yang, J. J. de Barbadillo, in *Liquid Metal Processing and Casting (LMPC)*, ASM International, Santa Fe **2005**.
[71] D. Yan-Wu, J. Zhou-Hua, L. Zheng, B. Li, *J. Iron Steel Res.* **2007**, *14*, 7.
[72] A. D. Patel, in *Liquid Metal Processing and Casting (LMPC)*, LMPC, Nancy **2007**, p.95.
[73] A. Kharicha, W. Schützenhöfer, A. Ludwig, R. Tanzer, in *Liquid Metal Processing and Casting (LMPC)*, LMPC, Nancy **2007**, p. 107.
[74] A. Kharicha, A. Mackenbrock, A. Ludwig, W. Schützenhöfer, V. Maronnier, M. Wu, O. Köser, R. Tanzer, in *Liquid Metal Processing and Casting (LMPC)*, LMPC, Nancy **2007**, p. 113.
[75] A. Kharicha, W. Schützenhöfer, A. Ludwig, R. Tanzer, M. Wu, *Steel Res. Int.* **2008**, *79*, 632.
[76] A. Rückert, H. Pfeifer, *Magnetohydrodynamics* **2009**, *45*, 527.
[77] A. Kharicha, W. Schützenhöfer, A. Ludwig, R. Tanzer, M. Wu, *Int. J. Cast Met. Res.* **2009**, *22*, 155.
[78] A. Jardy, D. Ablitzer, *Mater. Sci. Techol.* **2009**, *25*, 163.
[79] V. Weber, A. Jardy, B. Dussoubs, D. Ablitzer, S. Ryberon, V. Schmitt, S. Hans, H. Poisson, *Metall. Mater. Trans.* **2009**, *40*, 271.
[80] A. D. Patel, M. Gierula, D. J. Tallman, in *Liquid Metal Processing and Casting (LMPC)*, TMS, Santa Fe **2009**, p. 201.
[81] A. Kharicha, W. Schützenhöfer, A. Ludwig, R. Tanzer, in *Liquid Metal Processing and Casting (LMPC),* TMS, Santa Fe **2009**, p. 235.
[82] A. Kharicha, W. Schützenhöfer, A. Ludwig, G. Reiter, *Mater. Sci. Forum* **2010**, *649*, 229.
[83] A. Kharicha, A. Ludwig, M. Wu, in *EPD Congress*, Wiley, San Diego **2011**, p. 771.
[84] A. Kharicha, A. Ludwig, M. Wu, in *Liquid Metal Processing and Casting (LMPC)*, ASM International, Nancy **2011**, p. 73.
[85] A. D. Patel, in *Liquid Metal Processing and Casting (LMPC)*, ASM International, Nancy **2011**, p. 49.
[86] M. J. M. Krane, M. Fahrmann, J. Yanke, E. Escobar de Obaldia, K. Fezi, J. Busch, in *liquid metal processing and casting (LMPC)*, ASM International, Nancy, **2011**, p. 65.
[87] A. Kharicha, A. Ludwig, M. Wu, in *Liquid Metal Processing and Casting (LMPC)*, Nancy **2011**, p. 113.
[88] A. Kharicha, M. Wu, A. Ludwig, M. Ramprecht, H. Holzgruber, *CFD Modeling and Simulation in Materials*, Wiley Interscience, New Jersey, USA **2012**, p. 139.
[89] A. Kharicha, J. Korp, M. Wu, A. Ludwig, in *CLEANSTEEL8*, Budapest **2012**, p. 145.
[90] B. Li, F. Wang, F. Tsukihashi, *ISIJ Int.* **2012**, *52*, 1289.

[91] J. Yanke, K. Fezi, M. Fahrmann, M. J. M. Krane, in *Liquid Metal Processing and Casting (LMPC)*, Wiley, Austin **2013**, p. 47.
[92] M. Hugo, B. Dussoubs, A. Jardy, J. Escaffre, H. Poisson, in *Liquid Metal Processing and Casting (LMPC)*, Wiley, Austin **2013**, p. 79.
[93] K. M. Kelkar, S. V. Patankar, S. K. Srivatsa, R. S. Minisandram, D. G. Evans, J. J. de Barbadillo, R. H. Smith, R. C. Helmink, A. Mitchell, H. A. Sizek, in *Liquid Metal Processing and Casting (LMPC)*, Wiley, Austin **2013**, p. 3.
[94] A. Kharicha, M. Wu, A. Ludwig, in *Liquid Metal Processing and Casting (LMPC)*, **2013**, Wiley, Austin, p. 145.
[95] L. Rao, J.-H. Zhao, Z.-X. Zhao, G. Ding, M.-P. Geng, *J. Iron Steel Res.* **2014**, *21*, 644.
[96] Q. Wang, Z. He, B. LI, F. Tsukihashi, *Metall. Trans. B* **2014**, *45*, 2425.
[97] B. Li, Q. Wang, F. Wang, M. Chen, *JOM* **2014**, *66*, 1153.
[98] M. Eickhoff, N. Giesselmann, A. Rückert, H. Pfeifer, J. Tewes, J. Klöwer, in *2nd Int. Conf. on Ingot Casting, Rolling, and Forging*, Milan **2014**.
[99] J. Yanke, M. J. M. Krane, *Liquid Metal Processing and Casting (LMPC)*, Austin **2013**, p. 71.
[100] A. Kharicha, M. Wu, A. Ludwig, *ISIJ Int.* **2014**, *54*, 1621.
[101] Q. Wang, F. Wang, B. Li, F. Tsukihashi, *ISIJ Int.* **2015**, *55*, 1010.
[102] X. Wang, Y. Li, *Metall. Mater. Trans.* **2015**, *47*, p. 1475.
[103] K. Fezi, J. Yanke, M. J. M. Krane, *Metall. Mater. Trans.* **2015**, *46*, 766.
[104] N. Giesselmann, A. Rückert, M. Eickhoff, H. Pfeifer, J. Tewes, J. Klöwer, *ISIJ Int.* **2015**, *55*, 1408.
[105] E. Karimi-Sibaki, A. Kharicha, M. Wu, A. Ludwig, H. Holzgruber, B. Ofner, M. Ramprecht, in *Liquid Metal Processing and Casting (LMPC)*, Wiley, Austin **2013**, p. 13, DOI:10.1007/978-3-319-48102-9_2.
[106] E. Karimi-Sibaki, A. Kharicha, J. Bohacek, M. Wu, A. Ludwig, *Metall. Mater. Trans.* **2015**, *46*, 2049.
[107] A. Kharicha, E. Karimi-Sibaki, M. Wu, A. Ludwig, in *Liquid Metal Processing and Casting Conf. (LMPC)*, Wiley, Austin **2013**, p. 95, DOI: 10.1007/978-3-319-48102-9_13.
[108] Q. Wang, Z. He, G. Li, B. Li, C. Zhu, P. Chen, *Int. J. Heat Mass Trans.* **2017**, *104*, 943.
[109] M. Hugo, B. Dussoubs, A. Jardy, J. Escaffre, H. Poisson, *Metall. Mater. Trans B* **2016**, *47*, 2607.
[110] E. Karimi-Sibaki, A. Kharicha, M. Wu, A. Ludwig, H. Holzgruber, B. Ofner, A. Scheriau, M. Kubin, M. Ramprecht, *IOP Conf. Series: Mater. Sci. Eng.* **2016**, *143*, 012006. DOI:10.1088/1757-899X/143/1/012006
[111] E. Karimi-Sibaki, A. Kharicha, J. Korp, M. Wu, A. Ludwig, *Mater. Sci. Forum* **2014**, *790–791*, 396.
[112] A. Kharicha, E. Karimi-Sibaki, J. Bohacek, M. Wu, A. Ludwig, *Mater. Sci. Eng.* **2016**, *143*, 012003. DOI:10.1088/1757-899X/143/1/012003.
[113] E. Karimi-Sibaki, A. Kharicha, J. Bohacek, M. Wu, A. Ludwig, *Adv. Eng. Mater.* **2016**, *18*, 224.
[114] E. Karimi-Sibaki, A. Kharicha, M. Wu, A. Ludwig, H. Holzgruber, B. Ofner, M. Ramprecht, in *2nd Int. Conf. on Ingot Casting Rolling and Forging (ICRF)*, Milan **2014**.
[115] A. Kharicha, M. Wu, A. Ludwig, E. Karimi-Sibaki, *Metall. Mater. Trans.* **2016**, *47*, 1427.
[116] E. Karimi-Sibaki, *Multiphysics simulation of electroslag remelting process*, AV Akademikerverlag, Düsseldorf, Germany, **2016**.
[117] Q. Wang, B. Li, *Int. J. Prec. Eng. Manuf.* **2015**, *16*, 2193.
[118] K. Preis, I Bardi, O. Biro, C. Magele, W. Renhart, K. R. Richter, G. Vrisk, *IEEE Trans. Magn.* **1991**, *27*, 3798.
[119] H. Song, N. Ida, *IEEE Trans. Magn* **1991**, *27*, 4012.
[120] R. Mehrabian, M. Keane, M. C. Flemings, *Metall. Trans. B* **1970**, *1*, 1209.
[121] W. Kurz, B. Giovanola, R. Trivedi, *Acta. Metall.* **1986**, *34*, 823.
[122] A. Mitchell, in *Liquid Metal Processing and Casting (LMPC)*, IOP, Leoben **2015**, p. 13.
[123] A. Mitchell, *Ironmaking Steelmaking* **1974**, *3*, 172.
[124] H. Wang, Y. Zhong, Q. Li, Y. Fang, W. Ren, Z. Lei, Z. Ren, *Metall. Mater. Trans. B* **2017**, *48*, 655.
[125] D. A. R. Kay, R. J. Pomfret, *J. Iron Steel Inst.* **1971**, *209*, 962.
[126] N. Q. Minh, T. B. King, *Metall. Trans. B* **1979**, *10*, 623.
[127] M. Kato, K. Hasegawa, S. Nomura, M. Inouye, *Trans. ISIJ* **1983**, *23*, 618.
[128] M. Kawakami, T. Takenaka, M. Ishikawa, *Ironmaking Steelmaking* **2002**, *29*, 287.
[129] M. Kawakami, K. Nagata, M. Yamamura, N. Sakata, Y. Miyashita, K. S. Goto, *Testsu-to-Hagane* **1977**, *63*, 220.
[130] A. Mitchell, G. Beynon, *Metall. Trans.* **1971**, *2*, 3333.
[131] M. Etienne, *PhD Thesis*, UBC, **1970**.
[132] N. Nowack, K. Schwerdtfeger, D. Krause, *Arch. Eisenhüttenwes* **1982**, *53*, 463.
[133] R. Prange, K. Heusler, K. Schwerdtfeger, *Metall. Trans. B* **1984**, *15*, 281.
[134] K. Schwerdtfeger, W. Wepner, G. Pateisky, *Ironmaking Steelmaking* **1978**, *3*, 135.
[135] M. E. Fraser, A. Mitchell, *Ironmaking Steelmaking* **1976**, *5*, 279.
[136] M. E. Fraser, A. Mitchell, *Ironmaking Steelmaking* **1976**, *5*, 288.
[137] E. Karimi-Sibaki, A. Kharicha, M. Wu, A. Ludwig, *Mater. Sci. Eng.* **2016**, *143*, 012008. DOI:10.1088/1757899X/143/1/012008.

[138] E. Karimi-Sibaki, A. Kharicha, J. Bohacek, M. Wu, A. Ludwig, *J. App. Math. Comput*. **2017**, accepted for publication.
[139] E. Karimi-Sibaki, A. Kharicha, J. Bohacek, M. Wu, A. Ludwig, *Steel Res. Int*. **2017**, *88*, Article 1700011. DOI:10.1002/srin.201700011.
[140] A. Mitchell, *Ironmaking Steelmaking* **1975**, *3*, 198.
[141] M. Wu, J. Domitner, A. Ludwig, *Metall. Mater. Trans*. **2012**, *43*, 945.
[142] M. Wu, A. Ludwig, *Metall. Mater. Trans*. **2007**, *38*, 1465.
[143] M. Ahmadein, M. Wu, A. Ludwig, *J. Crystal Growth* **2015**, *417*, 65.
[144] M. Wu, A. Fjeld, A. Ludwig, *Comp. Mater. Sci*. **2010**, *50*, 32.